

Computer Physics Communications

A hybrid Eulerian-Lagrangian Vlasov method for nonlinear wave-particle interaction in weakly inhomogeneous magnetic field

--Manuscript Draft--

Manuscript Number:	
Article Type:	Computational Physics
Keywords:	Plasma Waves Vlasov Particle-in-cell Multi-scale Wave-particle interaction
Corresponding Author:	Bo Li Beihang University CHINA
First Author:	Jiangshan Zheng
Order of Authors:	Jiangshan Zheng Ge Wang Bo Li
Abstract:	We present a hybrid Eulerian-Lagrangian (HEL) Vlasov method for nonlinear resonant wave-particle interactions in weakly inhomogeneous magnetic field. The governing Vlasov equation is derived from a recently proposed resonance tracking Hamiltonian theory. It gives the evolution of the distribution function with a scale-separated Hamiltonian that contains the fast-varying coherent wave-particle interaction and slowly-varying motion about the resonance frame of reference. The hybrid scheme solves the fast-varying phase space evolution on Eulerian grid with an adaptive time step and interpolated differential operator and then advances the slowly-varying dynamics by Lagrangian method along the resonance trajectory. We apply the HEL method to study the frequency chirping of whistler-mode chorus wave in the magnetosphere and the self-consistent simulations reproduce the chirping chorus wave and give high-resolution phase space dynamics of energetic particles at low computational cost. The scale-separated HEL approach could provide additional insights of the wave instabilities and the wave-particle nonlinear coherence compared to the conventional Vlasov and particle-in-cell methods.
Suggested Reviewers:	Huasheng Xie ENN Science and Technology Development Co., Ltd. huashengxie@gmail.com Dr. Xie is a specialist in the area of plasma wave simulation. Guangye Chen Los Alamos National Laboratory gchen@lanl.gov Dr. Chen is a specialist in the area of multi-scale plasma kinetic simulation. Xin Tao University of Science and Technology of China xtao@ustc.edu.cn



Click here to access/download
LaTeX Source Files
cpc_all.tex

1
2
3
4
5
6
7
8
9
10
11
12
13
14
15
16
17
18
19
20
21
22
23
24
25
26
27
28
29
30
31
32
33
34
35
36
37
38
39
40
41
42
43
44
45
46
47
48
49
50
51
52
53
54
55
56
57
58
59
60
61
62
63
64
65

1
2
3
4
5
6
7
8
9
10 A hybrid Eulerian-Lagrangian Vlasov method for nonlinear
11 wave-particle interaction in weakly inhomogeneous magnetic field
12
13
14

15
16 Jiangshan Zheng^a, Ge Wang^{b,c}, Bo Li^a
17
18

19 ^a*School of Physics, Beihang University, Beijing, Beijing 100191, China*
20

21 ^b*Institute for Fusion Studies, University of Texas at Austin, Austin, Texas, 78712, USA*
22

23 ^c*Center for Plasma Theory and Computation, University of Wisconsin at Madison, Madison, Wisconsin 53706, USA*
24
25
26
27

28 **Abstract**
29
30
31

32 We present a hybrid Eulerian-Lagrangian (HEL) Vlasov method for nonlinear resonant wave-
33 particle interactions in weakly inhomogeneous magnetic field. The governing Vlasov equation is
34 derived from a recently proposed resonance tracking Hamiltonian theory. It gives the evolution of
35 the distribution function with a scale-separated Hamiltonian that contains the fast-varying coherent
36 wave-particle interaction and slowly-varying motion about the resonance frame of reference. The
37 hybrid scheme solves the fast-varying phase space evolution on Eulerian grid with an adaptive
38 time step and interpolated differential operator and then advances the slowly-varying dynamics
39 by Lagrangian method along the resonance trajectory. We apply the HEL method to study the
40 frequency chirping of whistler-mode chorus wave in the magnetosphere and the self-consistent
41 simulations reproduce the chirping chorus wave and give high-resolution phase space dynamics of
42 energetic particles at low computational cost. The scale-separated HEL approach could provide
43 additional insights of the wave instabilities and wave-particle nonlinear coherence compared to
44 the conventional Vlasov and particle-in-cell methods.
45
46
47
48

50
51
52
53
54
55
56
57 Email address: plasma@buaa.edu.cn (Bo Li)
58
59
60
61
62
63
64
65

1
2
3
4

1. Introduction

5 Wave-particle interaction, especially the nonlinear resonant interaction, is of great importance
6 and has been extensively discussed in a broad spectrum of plasma physics. In magnetically con-
7 fined fusion devices, the Alfvén wave instabilities are associated with mode frequency sweeping
8 [1, 2, 3, 4] and lead to premature ejection of alpha particles that deteriorate plasma confinement
9 [5]. The chorus waves in the planetary magnetosphere [6] are associated with various geophys-
10 ical activity like relativistic electron precipitation, X-ray microbursts, pulsating and diffuse auroras
11 [7, 8, 9]. Numerical models such as particle-in-cell [10, 11, 12], and ray tracing [13] can be applied
12 to study these wave-particle interactions and wave propagation. In particular, the Vlasov hybrid
13 simulation [14], electron hybrid model [15], and DAWN hybrid code [16] have been developed
14 for the numerical simulation of whistler-mode chorus in the Earth’s magnetosphere.
15

16 For the homogeneous plasmas [17, 18] or in the nonuniform regime with spatial symmetry
17 [19, 20, 21], the involved wave can be treated as standing wave with stationary fixed wave number
18 or mode number. In such cases, the interactions are confined to the periodic localized regions.
19 Consequently, the kinetic simulations in these scenarios are straightforward, benefiting from the
20 inherent periodicity of the system. When dealing with inhomogeneous scenarios, however, the pe-
21 riodicity no longer holds and even weak inhomogeneity can break the periodicity and significantly
22 modify the nonlinear wave-particle interaction. Although techniques like WKB approximation
23 [22] or slowly varying envelope approximation [23] can be applied to simplify the wave calcu-
24 lation, it is challenging to find a suitable approach to split the scales of the resonant particles
25 due to the nonlinear wave-particle interactions along the inhomogeneous magnetic field. Conse-
26 quently, the rapidly changing temporal and spatial scales come into play across all dimensions of
27 the resonant particle phase space, resulting in a significant computational cost than in homoge-
28 neous plasma settings. In addition, the traditional methods lack the required precision to describe
29 the fine structures of resonance particle phase space subject to the nonlinearity imposed by inho-
30 mogeneous magnetic fields and chirping waves.
31

32 To address these limitations, it is critical to decouple the multiple scales of wave and particle
33 motion to get a reduced description of the system. Recently, a Hamiltonian formulation using the
34 canonical coordinates and momenta has been developed in the reference frames moving at local
35 resonant velocities [24]. The wave phase is expanded about the local resonance center, which ef-
36 fectively decouples the multiple scales. The Hamiltonian consists of the fast-varying wave particle
37 interaction terms and the slowly-varying terms in the resonance frame moving along the resonance
38 trajectory. The particle slowly varying scale corresponds to the characteristic length of background
39 plasma inhomogeneity, and the angle variable in the fast varying dynamics can be treated as quasi-
40 periodic, similar to the treatment in a homogeneous plasma. Here we consider a delta f Vlasov
41 solver based on a hybrid Eulerian-Lagrangian (HEL) method [25] for solving the scale separated
42 Vlasov system. In the first step, a conservative form Interpolated Differential Operator (IDO)
43 method is applied to the Eulerian grid and an adaptive time step Runge-Kutta (RK) solver is used
44 to solve the fast varying dynamics in phase space. This provides high resolution simulation of
45 the formation and evolution of resonant structures arising from the rapidly changing wave-particle
46 interactions. The perturbed current is then integrated from the perturbed distribution function with
47 local equilibrium quantities. In the second step, the Lagrangian markers are sampled in slowly
48

varying domain and the trajectory of markers are solved by the RK method. Subsequently, the perturbed distribution is updated on the new marker coordinates. Finally, after completing the particle solver, the Vlasov system is coupled to the wave equation in the resonance frame through the perturbed current. We evolve the slowly varying wave envelope to the next time step with the second-order wave equation using the RK method. The first-order wave equation is also solved with an implicit upwind scheme. The nonlinear resonant interaction between frequency chirping chorus wave and energetic electrons in the Earth's magnetosphere is used as a benchmark for our simulation scheme. The bottleneck of our computation occurs within the Eulerian solver in two-dimensional space, which typically require hundreds of time iterations for a single Lagrangian time step for all markers. Nevertheless, the computational cost remains reasonable in comparison to conventional PIC simulations, where the number of sampling points is at least orders of magnitude greater than the HEL method. Consequently, the PIC simulations typically require billions of particles [26, 15], but the phase space resolution is significantly lower than that in the HEL method.

The paper is organized as follows. In section 2, we present the HEL scheme for the scale separated Vlasov system. In section 3, we present the numerical method for solving the slowly varying wave envelope. Section 4 provides a detailed benchmark of the simulation code. Finally, the conclusion is provided in section 5.

2. The Hybrid Eulerian-Lagrangian Solver for the Vlasov system

For the nonlinear resonant wave-particle interaction in weakly inhomogeneous magnetic field, the Hamiltonian in the reference frames moving at local resonant velocities can be formulated in terms of the canonical variables ξ, Ω for the fast varying dynamics and ϑ, \mathcal{J} for the slowly varying scales [24]. Then the evolution of perturbed distribution function $\delta f(\vartheta, \mathcal{J}; \xi, \Omega; s, t)$ for the energetic particles is

$$\frac{\partial \delta f}{\partial t} + \frac{ds}{dt} \frac{\partial \delta f}{\partial s} + [\delta f, H]_{\vartheta, \mathcal{J}} + [\delta f, H]_{\xi, \Omega} = \mathcal{S}, \quad (1)$$

where s is the distance along the magnetic field line and the Poisson brackets are defined as

$$[f, g]_{x,y} = \frac{\partial f}{\partial x} \frac{\partial g}{\partial y} - \frac{\partial f}{\partial y} \frac{\partial g}{\partial x}. \quad (2)$$

Here the source term $\mathcal{S} = -[f_0, \delta H]_{\vartheta, \mathcal{J}} - [f_0, \delta H]_{\xi, \Omega}$ where f_0 is the equilibrium distribution function and δH denotes the perturbed Hamiltonian due to the resonant wave-particle interactions. Note that the derivatives of δH with respect to the slowly varying coordinates ϑ and \mathcal{J} can be neglected due to the separation of perturbation and equilibrium scales. Besides, $\partial f_0 / \partial \xi$ is vanished since f_0 does not generally depend on the fast varying angle coordinate ξ . Thus, the source term can be simplified as

$$\mathcal{S} = \frac{\partial \delta H}{\partial \xi} \frac{\partial f_0}{\partial \Omega}. \quad (3)$$

The variation of the angular coordinate ϑ is negligible due to the weakly inhomogeneous nature of the plasmas, while the dynamics of \mathcal{J}, Ω , and ξ remain entirely unaffected by ϑ . Therefore we

neglect the term $\dot{\vartheta}$ in the Vlasov equation and the Poisson bracket becomes

$$[\delta f, H]_{\vartheta, \mathcal{J}} \simeq -\dot{\mathcal{J}} \frac{\partial \delta f}{\partial \mathcal{J}} \quad (4)$$

where the dot denotes the time derivative.

We now implement the hybrid method to solve the Vlasov system, which has been structured to separate the fast and slowly varying scales within the Hamiltonian theory. We utilize the Eulerian method to model the fast-varying phase space ξ, Ω and employ the Lagrangian method to model the slowly varying coordinates \mathcal{J} and the resonance frame coordinate s . The distribution function is written as [25]

$$\delta f(\xi, \Omega, \mathcal{J}, s, t) = \sum_{k,l} g_{k,l}(t, \xi, \Omega) \delta(s - s_k(t), \mathcal{J} - \mathcal{J}_l), \quad (5)$$

where $g_{k,l}(t, \xi, \Omega)$ represents the distribution function in ξ, Ω space with k and l denoting the indices of the Lagrangian markers. Then the evolution equation for $g_{k,l}(t, \xi, \Omega)$ for each marker labeled by k and l is

$$\frac{\partial g}{\partial t} + [g, H]_{\xi, \Omega} = \mathcal{S}. \quad (6)$$

Here we omit the index k and l of g for convenience.

In the Lagrangian step, it is essential for the marker to move with the resonance frame throughout the spatial domain, i.e.,

$$\dot{s}_k = v_r(s_k(t)), \quad (7)$$

where v_r is the resonant velocity. The motion equation for slowly varying coordinate \mathcal{J} is

$$\dot{\mathcal{J}} = [\mathcal{J}, H]_{\vartheta, \mathcal{J}}. \quad (8)$$

2.1. The Eulerian step

We first solve the fast-varying phase space dynamics for each Lagrangian marker at s_k, \mathcal{J}_l . For the numerical treatment, the Vlasov equation (6) is expressed as

$$\frac{\partial g}{\partial t} + m \frac{\partial g}{\partial \xi} - n \frac{\partial g}{\partial \Omega} = \mathcal{S}, \quad (9)$$

where

$$m(\xi, \Omega) = \frac{\partial H}{\partial \Omega}, \quad n(\xi, \Omega) = \frac{\partial H}{\partial \xi}. \quad (10)$$

To achieve high-order accuracy, we apply the IDO method [27] to solve the 2D Vlasov equation in ξ, Ω domain. The derivatives of g with respect to ξ and Ω are then approximated by the derivatives of a second-order polynomial G [27]. The discretized form of the Vlasov equation (9) becomes

$$\begin{aligned} \left. \frac{\partial g}{\partial t} \right|_{i,j} &= -m_{i,j} \left. \frac{\partial}{\partial \xi} G(\xi; g_{i,j}, g_{i+1,j}, \rho_{i+\frac{1}{2},j}) \right|_{i,j} \\ &\quad + n_{i,j} \left. \frac{\partial}{\partial \Omega} G(\Omega; g_{i,j}, g_{i,j+1}, \kappa_{i,j+\frac{1}{2}}) \right|_{i,j} \\ &\quad + \mathcal{S}_{i,j}, \end{aligned} \quad (11)$$

where G is a second-order polynomial, $g_{i,j}$ are function values on the grid, $\rho_{i+\frac{1}{2},j} = \int_{\xi_i}^{\xi_{i+1}} g_j(\xi) d\xi$ and $\kappa_{i,j+\frac{1}{2}} = \int_{\Omega_j}^{\Omega_{j+1}} g_i(\Omega) d\Omega$ are the integrated function values over the grid. Here i and j denote the grid index for ξ and Ω , respectively. The grid and interpolation are demonstrated in Fig. 1. Integrating Eq. (9) along ξ and Ω over the grid interval yields the time evolution of the integral

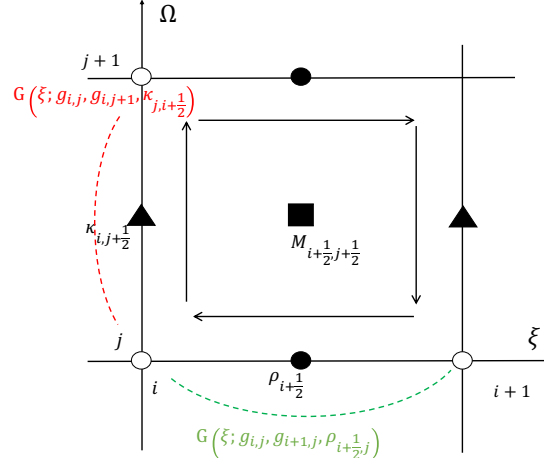


Figure 1: The interpolating functions and integrated values in ξ, Ω domain.

values [27]

$$\begin{aligned}
 \frac{\partial \rho}{\partial t} \Big|_{i+\frac{1}{2},j} &= \int_{\xi_i}^{\xi_{i+1}} [-m_j(\xi) \frac{\partial g}{\partial \xi} \Big|_j (\xi) + n_j(\xi) \frac{\partial g}{\partial \Omega} \Big|_j (\xi) + S_j(\xi)] d\xi, \\
 \frac{\partial \kappa}{\partial t} \Big|_{i,j+\frac{1}{2}} &= \int_{\Omega_j}^{\Omega_{j+1}} [-m_i(\Omega) \frac{\partial g}{\partial \xi} \Big|_i (\Omega) + n_i(\Omega) \frac{\partial g}{\partial \Omega} \Big|_i (\Omega) + S_i(\Omega)] d\Omega.
 \end{aligned} \tag{12}$$

The third-order central interpolation scheme is applied to approximate the functions m and n along the ξ and Ω dimension and the interpolating stencil is used to approximate the derivatives,

$$\begin{aligned}
 \frac{\partial g}{\partial \xi} \Big|_j (\xi) &\simeq G \left(\xi; \frac{\partial g}{\partial \xi} \Big|_{i,j}, \frac{\partial g}{\partial \xi} \Big|_{i+1,j}, g_{i+1,j} - g_{i,j} \right), \\
 \frac{\partial g}{\partial \Omega} \Big|_j (\xi) &\simeq G \left(\xi; \frac{\partial g}{\partial \Omega} \Big|_{i,j}, \frac{\partial g}{\partial \Omega} \Big|_{i+1,j}, \frac{\partial \rho}{\partial \Omega} \Big|_{i+\frac{1}{2},j} \right), \\
 \frac{\partial g}{\partial \Omega} \Big|_i (\Omega) &\simeq G \left(\Omega; \frac{\partial g}{\partial \Omega} \Big|_{i,j}, \frac{\partial g}{\partial \Omega} \Big|_{i,j+1}, g_{i,j+1} - g_{i,j} \right), \\
 \frac{\partial g}{\partial \xi} \Big|_i (\Omega) &\simeq G \left(\Omega; \frac{\partial g}{\partial \xi} \Big|_{i,j}, \frac{\partial g}{\partial \xi} \Big|_{i,j+1}, \frac{\partial \kappa}{\partial \xi} \Big|_{i,j+\frac{1}{2}} \right),
 \end{aligned} \tag{13}$$

1
2
3 where

$$\begin{aligned} \frac{\partial \rho}{\partial \Omega} \Big|_{i+\frac{1}{2},j} &\simeq \frac{\partial}{\partial \Omega} G(\Omega; \rho_{i+\frac{1}{2},j}, \rho_{i+\frac{1}{2},j+1}, M_{i+\frac{1}{2},j+\frac{1}{2}}) \Big|_{i+\frac{1}{2},j}, \\ \frac{\partial \kappa}{\partial \xi} \Big|_{i,j+\frac{1}{2}} &\simeq \frac{\partial}{\partial \xi} G(\xi; \kappa_{i,j+\frac{1}{2}}, \kappa_{i+1,j+\frac{1}{2}}, M_{i+\frac{1}{2},j+\frac{1}{2}}) \Big|_{i,j+\frac{1}{2}}. \end{aligned} \quad (14)$$

10
11 The time evolution of the surface integral $M_{i+\frac{1}{2},j+\frac{1}{2}} = \int_{\xi_i}^{\xi_{i+1}} \int_{\Omega_j}^{\Omega_{j+1}} g(t, \xi, \Omega) d\xi d\Omega$ is given by [27]
12

$$\begin{aligned} \frac{\partial M}{\partial t} \Big|_{i+\frac{1}{2},j+\frac{1}{2}} &= \int_{\xi_i}^{\xi_{i+1}} n_{j+1}(\xi) g_{j+1}(\xi) d\xi - \int_{\Omega_j}^{\Omega_{j+1}} m_{i+1}(\Omega) g_{i+1}(\Omega) d\Omega \\ &\quad - \int_{\xi_i}^{\xi_{i+1}} n_j(\xi) g_j(\xi) d\xi + \int_{\Omega_j}^{\Omega_{j+1}} m_i(\Omega) g_i(\Omega) d\Omega \\ &\quad + \iint \mathcal{S}(\xi, \Omega) d\xi d\Omega, \end{aligned} \quad (15)$$

23 where the integral of the source term is solved by trapezoidal integration.

24 Equations (11), (12), and (15) are a set of ordinary differential equations that can be solved by
25 the RK method. For the boundary conditions, the values of the perturbed distribution vanish at the
26 Ω boundaries and the distribution functions in the resonant frame are assumed to be periodic in
27 the angle variable ξ ,

$$g(\xi, \Omega, t) = g(\xi + 2\pi, \Omega, t). \quad (16)$$

31 Note that the periodic boundary conditions are valid only when the resonance does not deviate too
32 far away from the resonance frame of reference initially set in the simulation.
33

35 2.2. The Lagrangian step

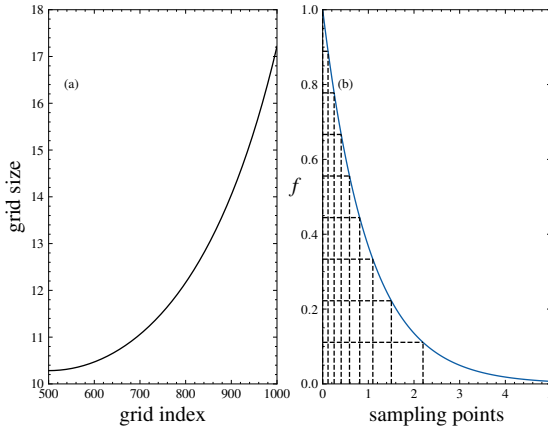
36 To initially position the markers in the spatial domain, we place them on the fixed grid denoted
37 as s_k . To ensure that each marker updates over an identical time step, we implement nonuniform
38 grid along the magnetic field line, as shown in Fig. 2(a). Initially, we calculate the transit time of
39 a marker over the entire spatial domain,
40

$$T = \int_{s_1}^{s_N} \frac{ds}{v_r(s)}, \quad (17)$$

46 where $v_r(s)$ is the local resonant velocity that has been predetermined from the background equi-
47 librium parameter. Then the simulation time step is set as $\Delta t = T/N$ with N the total number of
48 sampling points/grids. Finally, the initial spatial coordinates of the markers are set according to
49 Eq. (7) which gives the trajectory of the marker,
50

$$s_{k+1} = s_k + \int_t^{t+\Delta t} v_r(s_k(t)) dt, \quad (18)$$

52 where $k = 1, 2, 3, \dots, N$. Utilizing this nonuniform grid, the Lagrangian markers initially positioned
53 on the grid advance to the next adjacent grid point after a time interval Δt . Thus we successively
54



18
19 Figure 2: (a) Nonuniform spatial grid obtained from resonance velocity. (b) Sampling point for \mathcal{J} .
20

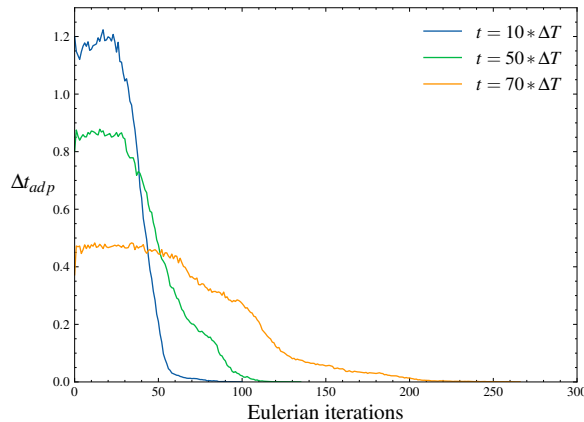
21 push the distribution $g_{k,l}(\xi, \Omega)$ from s_k to the next grid s_{k+1} for each time interval Δt . After pushing
22 the Lagrangian marker from the n^{th} to the $n + 1^{\text{th}}$ time step, the Hamiltonian is re-calculated by
23 the equilibrium quantities at the new location of s and \mathcal{J} , which are needed for evolving the
24 distribution in $\xi - \Omega$ space at the next time step.
25

26 For the Lagrangian markers, the sampling point for \mathcal{J} is chosen to ensure a uniform sampling
27 to the initial equilibrium distribution f_0 ,
28

$$30 \quad 31 \quad 32 \quad 33 \quad 34 \quad 35 \quad 36 \quad 37 \quad 38 \quad 39 \quad 40 \quad 41 \quad 42 \quad 43 \quad 44 \quad 45 \quad 46 \quad 47 \quad 48 \quad 49 \quad 50 \quad 51 \quad 52 \quad 53 \quad 54 \quad 55 \quad 56 \quad 57 \quad 58 \quad 59 \quad 60 \quad 61 \quad 62 \quad 63 \quad 64 \quad 65$$

$$\mathcal{J}_l \rightarrow \int^{\mathcal{J}_l} f_0 d\mathcal{J} = l/N, \quad (19)$$

where N is the total number of sampling points for \mathcal{J} . An illustration is shown in Fig. 2(b). The evolution of \mathcal{J} in Eq. (8) is simply solved by the RK method.



52 Figure 3: Variation of time step Δt_{adp} with the number of iterations for Eulerian calculation.
53

54 Since the evolution in the ξ, Ω phase space is much faster than that in the s, \mathcal{J} domain, we
55 employ a larger fixed time step Δt for the Lagrangian calculations and a much smaller adaptive
56 time step, Δt_{adp} , for resolving the rapidly varying dynamics in the Eulerian domain. The time steps
57

Δt_{adp} are adaptively determined through real-time error analysis using the adaptive RK method and satisfy

$$\sum_1^N \Delta t_{\text{adp}} = \Delta t , \quad (20)$$

where N is the total number of iterations within one Δt . As shown in Fig. 3, Δt_{adp} is continuously adjusted and refined, consistently reducing its value whenever the numerical error exceeds the predefined error threshold. As the system undergoes nonlinear evolution, the time step Δt_{adp} undergoes further refinement, automatically increasing the number of iterations within a single Δt interval. This highlights the clear advantage of adaptive hybrid methods in significantly improving computational efficiency.

Finally, we also implement a uniform grid and sample Lagrangian markers on s to validate the effectiveness of our nonuniform grid approach. After a given time step Δt the markers deviated from the fixed grid, thus we need to interpolate the distribution function and its derivatives required in the IDO scheme from the adjacent marker to the fixed s grid. These procedures closely resemble those of the semi-Lagrangian method [28, 29]. Following interpolation, the markers re-align with the grid, and the next iteration starts from the grid point. As shown in Fig. 4, the wave amplitudes calculated from the two approaches converge as the smaller grid sizes are used for the uniform grid with interpolation.

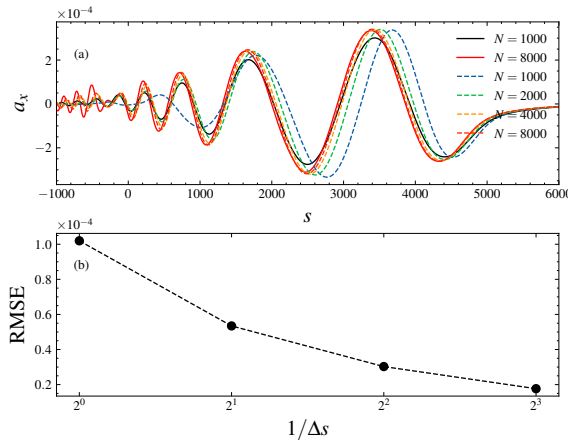


Figure 4: (a) Wave amplitude from semi-Lagrangian method with linear interpolation of distribution at different uniform grid sizes (dashed-line) and the nonuniform grid (solid line). (b) Root-mean-square error at different uniform grid sizes compared to the nonuniform grid of $N = 8000$.

3. Wave Equation

We proceed to integrate the HEL Vlasov solver with the wave equation, enabling us to self-consistently investigate resonant wave-particle interactions. Here we focus on the interaction between energetic electrons and chorus waves in the Earth's magnetosphere. Chorus waves are circularly polarized electromagnetic waves that propagate along the Earth's dipole magnetic field.

The vector potential $\mathbf{A}(s, t)$ representing the transverse wave is expressed as follows:

$$\mathbf{A}(s, t) = \mathbf{a}(s, t)e^{i\phi_f}, \quad (21)$$

where ϕ_f is the fast varying phase and $\mathbf{a}(s, t)$ is the slowly varying envelope of the wave packet. The normalized second-order wave equation for the chorus in the resonance frame is

$$\begin{aligned} & \frac{\partial^2 a}{\partial t^2} - \frac{\partial^2 a}{\partial s^2} + 2i\omega_l \frac{\partial a}{\partial t} + 2ik_l \frac{\partial a}{\partial s} + \\ & \frac{\omega_{pe}^2 \omega_{ce}}{(\omega_{ce} - \omega_l)} \int_0^t d\tau \frac{\partial a}{\partial \tau} e^{-i(\omega_l - \omega_{ce})(t-\tau)} = j_p, \end{aligned} \quad (22)$$

where $a = a_x + ia_y$ with x and y the directions perpendicular to the magnetic field. Note that the most unstable frequency ω_l and wave number k_l used in the simulation are obtained from the linear whistler dispersion relation. The plasma frequency $\omega_{pe}(s)$ and electron gyrofrequency $\omega_{ce}(s)$ are determined by the background plasma density and magnetic field profile along the magnetic field line. The plasma current is a combination of contributions from both cold electrons and energetic electrons. The cold electron current can be analytically integrated. The energetic electron current j_p is obtained from the perpendicular velocity moment of energetic particle distribution,

$$j_p(s, t) = -ek_l(t) \iiint v_\perp f(\xi, \Omega; \mathcal{J}; s, t) e^{i\xi} d\xi d\Omega d\mathcal{J}. \quad (23)$$

The second-order wave equation (22) can be expressed as a system of first-order ordinary differential equations,

$$\begin{aligned} \frac{dy_0}{dt} &= y_1 \\ \frac{dy_1}{dt} &= -2i\omega_l y_1 + \frac{\partial^2 y_0}{\partial s^2} - 2ik_l \frac{\partial y_0}{\partial s} - \frac{\omega_{pe}^2 \omega_{ce}}{\omega_{ce} - \omega_l} y_2 + j_p \\ \frac{dy_2}{dt} &= y_1 - i(\omega_l - \omega_{ce}) y_2, \end{aligned} \quad (24)$$

where

$$\begin{aligned} y_0 &= a(s, t), \\ y_1 &= \frac{\partial a(s, t)}{\partial t}, \\ y_2 &= e^{-i(\omega_l - \omega_{ce})t} \int_0^t d\tau \frac{\partial a}{\partial \tau} e^{i(\omega_l - \omega_{ce})\tau}. \end{aligned} \quad (25)$$

The grid for solving the wave equation is the same as the grid for Lagrangian markers. For the nonuniform grid, a linear combination of finite difference scheme is employed and the first and second order spatial derivatives are given by

$$\frac{\partial f}{\partial z} \approx \frac{f(z_k) - f(z_{k-1})}{z_k - z_{k-1}} + \frac{f(z_k) - f(z_{k+1})}{z_k - z_{k+1}} - \frac{f(z_{k+1}) - f(z_{k-1})}{z_{k+1} - z_{k-1}}, \quad (26)$$

1
2
3
4
and

$$\frac{\partial^2 f}{\partial z^2} \approx 2 \left(\frac{f(z_{k-1})}{(z_{k-1} - z_k)(z_{k-1} - z_{k+1})} + \frac{f(z_k)}{(z_k - z_{k+1})(z_k - z_{k-1})} + \frac{f(z_{k+1})}{(z_{k+1} - z_k)(z_{k+1} - z_{k-1})} \right). \quad (27)$$

9 The ordinary differential equations (24) are then advanced in time using the RK method.
10
11
12
13

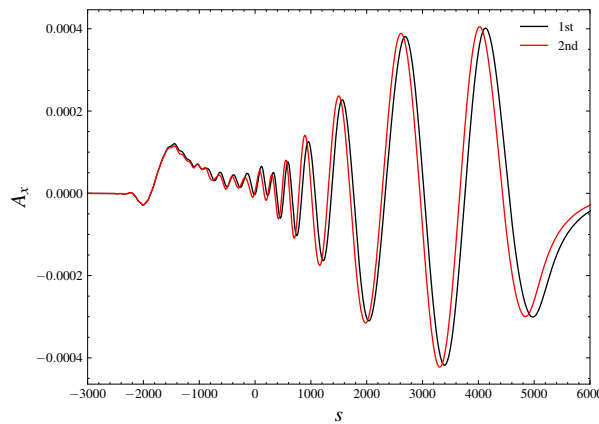
To check the contribution of the second order derivatives of slowly varying kernel $a(s, t)$ in the wave equation (22), we further simplify the integral term and obtain the first-order advective wave equation
14
15
16

$$\frac{\partial a}{\partial t} + v_g \frac{\partial a}{\partial s} = \frac{2\pi v_g}{k_l} j_p, \quad (28)$$

17 where $v_g(s)$ is the linear group velocity determined by the whistler dispersion relation. Using the
18 implicit upwind scheme, the discretized form of Eq. (28) is
19

$$a_k^{n+1} = a_k^n - u_k \cdot (a_k^{n+1} - a_{k-1}^{n+1}) \frac{\Delta t}{\Delta s} + S_k^n \Delta t \quad (29)$$

20 where the subscript k is the spatial grid index and the superscript n is the time index. Here u_k
21 denotes $v_g(s = s_k)$ and S is the source term on the right-hand-side of Eq. (28). For the wave
22 packet traveling from left to right with a group velocity $v_g > 0$, we apply a fixed noisy initialization
23 condition at the left end and absorption boundary conditions at the other end of the domain. Figure
24 demonstrates that the first-order wave equation provides a strong approximation to the second-
25 order wave equation. Consequently, the second-order term in Eq. (22) may be neglected when
26 simulating the onset of chorus wave frequency chirping for the sake of computational efficiency.
27
28
29
30
31
32



48
49 Figure 5: Wave amplitudes calculated from the second-order and first-order wave equations during the onset of
50 chorus wave frequency chirping.

51 52 53 4. Benchmark Results for the Onset of Rising Tone Chorus 54

55 We proceed with a series of simulations, employing our method to investigate the onset of the
56 whistler-mode chorus in the magnetosphere. The instability of the whistler wave typically arises
57
58

from the electron temperature anisotropy [30, 31] and the growth rate can be derived from the linear resonance condition. In our simulation, the energetic electron distribution is bi-Maxwellian at the magnetic equator,

$$f_0(\Omega, \mathcal{J}) = \frac{\omega_{ce0}}{(2\pi)^{3/2} v_{\perp 0}^2 v_{\parallel 0}} \cdot \exp\left(-\frac{k_l^2(\Omega + \Pi_i)^2}{2v_{\parallel 0}^2}\right) \cdot \exp\left(-\frac{(\mathcal{J} + \Omega + \Pi_i)\omega_{ce0}}{v_{\perp 0}^2}\right), \quad (30)$$

where $v_{\parallel 0}$ and $v_{\perp 0}$ are the parallel and perpendicular thermal velocity of energetic electrons, and the subscript 0 denotes the magnetic equator. The background magnetic field strength near the equator is approximated by a parabolic function [16]

$$B(\lambda) = B_0(1 + R_a\lambda^2), \quad (31)$$

where R_a is the inhomogeneity parameter of the magnetic dipole field, B_0 is the magnetic field strength at the equator, and λ is the magnetic latitude. For the dipole field, $B_0 = B_{0g}/L^3$ where $B_{0g} \approx 0.3$ G is the magnetic field of the Earth at the equator and L is the L-shell of the magnetic field line. The background electron density along the magnetic field line is fit to a power law [32],

$$n(\lambda) = n_0(1 + R_b\lambda^2), \quad (32)$$

where R_b represents the background cold plasma density inhomogeneity. For the normalization in the simulation, we use electron mass m_e , electron charge e , speed of light c and background electron plasma frequency at the magnetic equator ω_{pe0} to normalize mass, charge, velocity and frequency. Then the units for the other quantities can be derived. For example, the length s is normalized to c/ω_{pe0} and the vector potential A to $m_e c^2/e$.

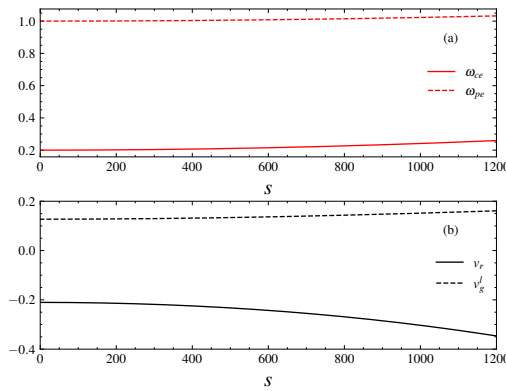


Figure 6: (a) Background magnetic field and density profile. (b) Resonant and linear group velocity profile along the magnetic field line.

Table 1: Magnetic field and plasma parameters used in the simulation.

L-shell of the magnetic field line	5
Magnetic field inhomogeneity R_a	4.5
Background cold plasma density inhomogeneity R_b	1.0
Background electron gyrofrequency and plasma frequency at the equator	$\omega_{ce0} = 43929.6 \text{ rad/s}$
Ratio of energetic to cold electron density at the equator	$\omega_{pe0} = 5\omega_{ce0}$
Parallel and perpendicular thermal velocity of energetic electrons	$n_{h0} = 0.002$
Size of the simulation domain	$v_{\perp 0} = 0.3c$
	$v_{\parallel 0} = 0.15c$
	$\lambda \in [-15^\circ, 15^\circ]$
	$s \in [-6115, 6115]c/\omega_{pe0}$

4.1. Simulation configuration

In conventional PIC simulations, the inhomogeneity ratio R_a is often increased by one or two order of magnitudes to reduce the simulation cost. Benefiting from the scale-separated HEL scheme, the realistic parameters for the Earth's dipole field can be used in our numerical simulation. The basic parameters of our simulation are given in Table (4.1) and the profiles of the background parameter are shown in Fig. 6. The most unstable wave frequency ω_l used in the simulation is determined from the linear growth rate γ_l [33],

$$\gamma_l(s) = \frac{\sqrt{2\pi}\omega_{ce}v_g n_{h0}\omega_{pe0}^2}{4k_l^2 v_{\parallel 0}} e^{-\frac{(\omega_l - \omega_{ce})^2}{2k_l^2 v_{\parallel 0}}} \cdot \left(\frac{T_{\perp 0}}{T_{\parallel 0}} \frac{\omega_{ce0} - \omega_l}{\omega_{ce0}} - 1 \right), \quad (33)$$

where n_{h0} is the density ratio of the energetic electrons to the background cold plasma at the magnetic equator, the wave number k_l satisfies the linear whistler dispersion relation

$$\frac{c^2 k_l^2(s)}{\omega_l^2} = 1 + \frac{\omega_{pe}^2(s)}{\omega_l(\omega_{ce}(s) - \omega_l)}, \quad (34)$$

and v_g is the linear whistler group velocity,

$$v_g(s) = \frac{2k_l(s)c^2}{2\omega_l + \omega_{pe}^2(s)\omega_{ce}(s)/(\omega_{ce}(s) - \omega_l)^2}. \quad (35)$$

The temperature is given by the thermal velocity shown in Tab. (4.1). For the parameters in Tab. (4.1), the most unstable growth rate is $\gamma_l \simeq 3.24 \times 10^{-4}$ and the corresponding frequency is $\omega_l = 0.061$, as shown by a scan of the parameter given in Fig. 7. For the typical runs, we set the number of grids for wave solver to be 1001 which is equal to the number of sampling points in s . In the \mathcal{J} dimension, we employ a delta function with only a single sampling point for \mathcal{J} . In the case of a non-delta distribution, tens of sampling points prove to be sufficient for \mathcal{J} sampling. For the ξ, Ω domain, the Eulerian grids are 31×401 for $\xi \in [0, 2\pi]$ and $\Omega \in [-0.1, 0.1]$.

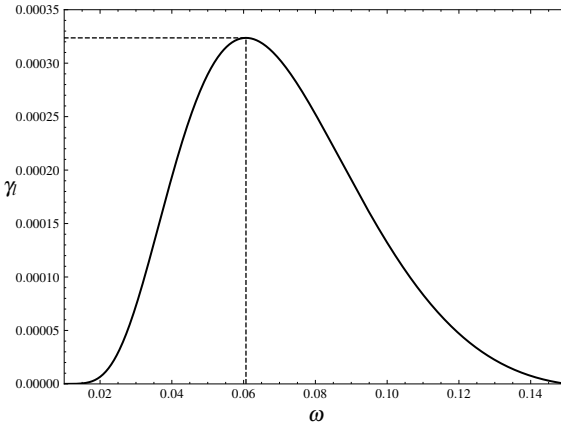


Figure 7: Linear growth rate γ_l with respect to ω_l for the simulation parameters. The initial frequency of the wave is obtained from the most unstable frequency indicated by the vertical black line.

4.2. Benchmarks results

The linear physics are quantitatively verified in Fig. 8, where we calculate the growth rate and the velocity of the maximum wave amplitude location before nonlinear effects become dominant. The trajectory of the propagating wave packet is determined theoretically using the integral of the linear group velocity,

$$s(t) = s(0) + \int_0^t v_g(s(\tau)) d\tau. \quad (36)$$

For the simulation, we track the movement of the maximum amplitude point. As shown in Fig. 8(a), the wave peak indeed propagates at the linear group velocity during the linear stage. The amplitude growth of the wave peak along its propagation path is shown in Fig. 8(b) and the growth rate is estimated by [26]

$$\gamma = \frac{1}{t_1 - t_0} \log \frac{|a(s_1, t_1)|}{|a(s_0, t_0)|}, \quad (37)$$

where s_0 and s_1 are the points along the propagation path. The growth rate calculated from Eq. (37) is $\gamma \simeq 3.21 \times 10^{-4}$, which agrees with the theoretical linear growth rate shown in Fig. 7.

In the nonlinear stage, the distribution of trapped electrons forms a hole structure in $\xi - \Omega$ phase space. This phase space hole contributes to the nonlinear current, which in turn triggers the nonlinear frequency-chirping chorus wave. The trapped electron experiences an oscillatory force from the wave and a noninertial force from background inhomogeneity. The forces can be described by a potential well with the form $\sin \xi + \alpha \xi$ with the parameter α as an inhomogeneity ratio [34, 35]. From the inflection point of the potential well, we can find the X point of the phase space trajectory,

$$\xi_x = -\arcsin \alpha, \quad (38)$$

and the C point of the trajectory is obtained from the energy on the separatrix $e_{\text{spx}} = \sin \xi_x + \alpha \xi_x$,

$$\sin \xi_c + \alpha \xi_c = e_{\text{spx}}. \quad (39)$$

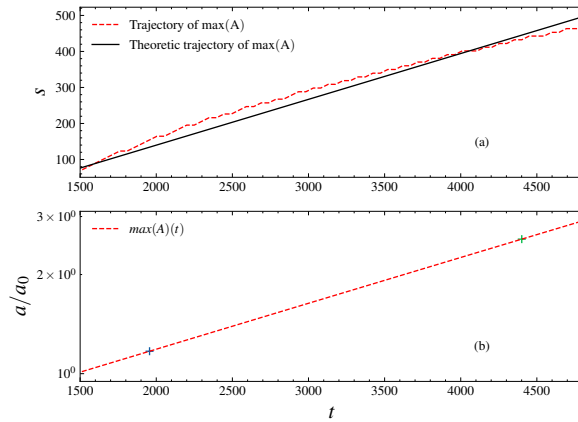


Figure 8: (a) Propagation trajectory of the linear wave packet with the maximum amplitude from the simulation (dashed line) and theory (solid line). (b) Growth of the wave peak amplitude with time along wave propagation path. The green crosses are the points used to calculate the growth rate.

The shape of the hole, specifically its boundary, can be analytically described as follows [34]:

$$\Omega(\xi) = \pm \frac{\omega_b}{k^2} \sqrt{2(e_{\text{spx}} - \cos \xi - \alpha \xi)}, \quad (40)$$

where k is the wave number and ω_b is the trapped particle bounce frequency. Using the simulation data we obtain the values of $k \simeq 0.649$, $\omega_b \simeq 0.007$, and $\alpha \simeq 0.08$ at a specific location $s \simeq 2107$. Then the boundary of the hole can be obtained using Eq. (40). As shown in Fig. 9, the shape of the hole in the nonlinear simulation closely matches the theoretical predictions.

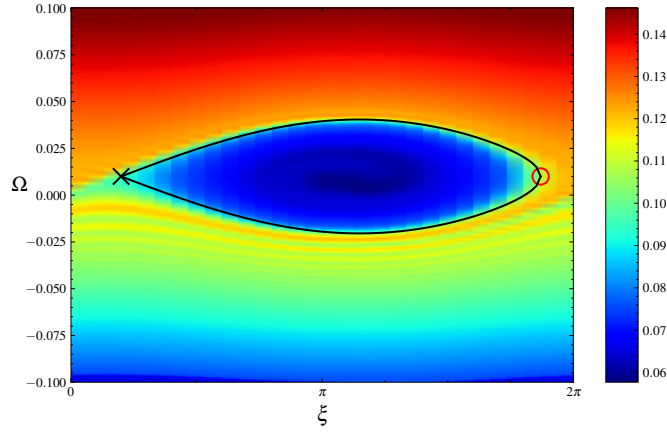


Figure 9: Phase-space hole formed by trapped electrons at $s \simeq 2107$ in the wave field. The X, C points on the left and right ends and the boundary of the hole (black solid line) are obtained from theory.

5. Conclusion

In summary, we have developed a hybrid Eulerian-Lagrangian method tailored for the resonance tracking Vlasov system for understanding of nonlinear resonant wave-particle interactions

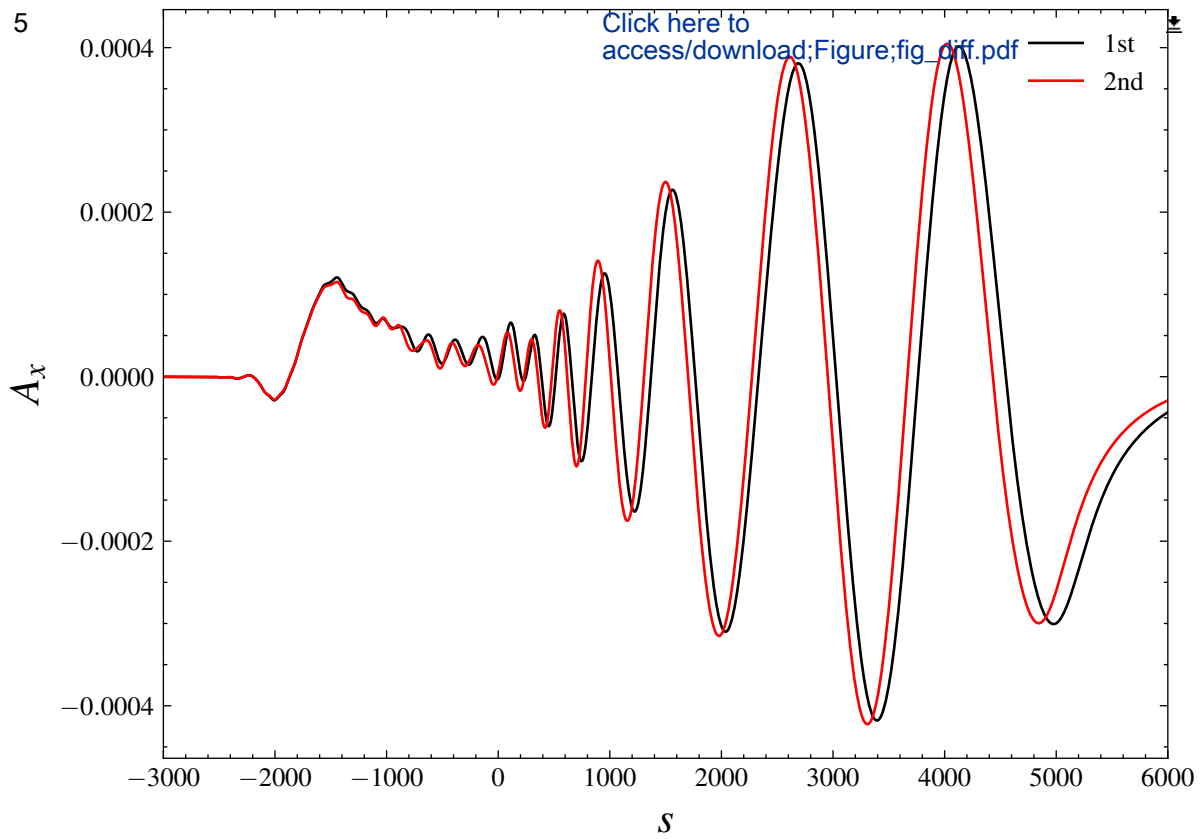
1
2
3 in the inhomogeneous magnetic fields. This HEL method effectively separates the fast and slowly
4 varying dynamics of nonlinear resonant wave-particle interactions and therefore significantly re-
5 duces the computational cost compared to the conventional Vlasov and particle-in-cell methods.
6 To validate the scale-separated HEL approach, we have conducted self-consistent simulations fo-
7 cusing on the whistler-mode chorus in the Earth's magnetosphere using realistic parameters. The
8 results not only exhibit agreement with the linear predictions but also reveal high-resolution phase
9 space structures of resonant energetic particles.
10
11

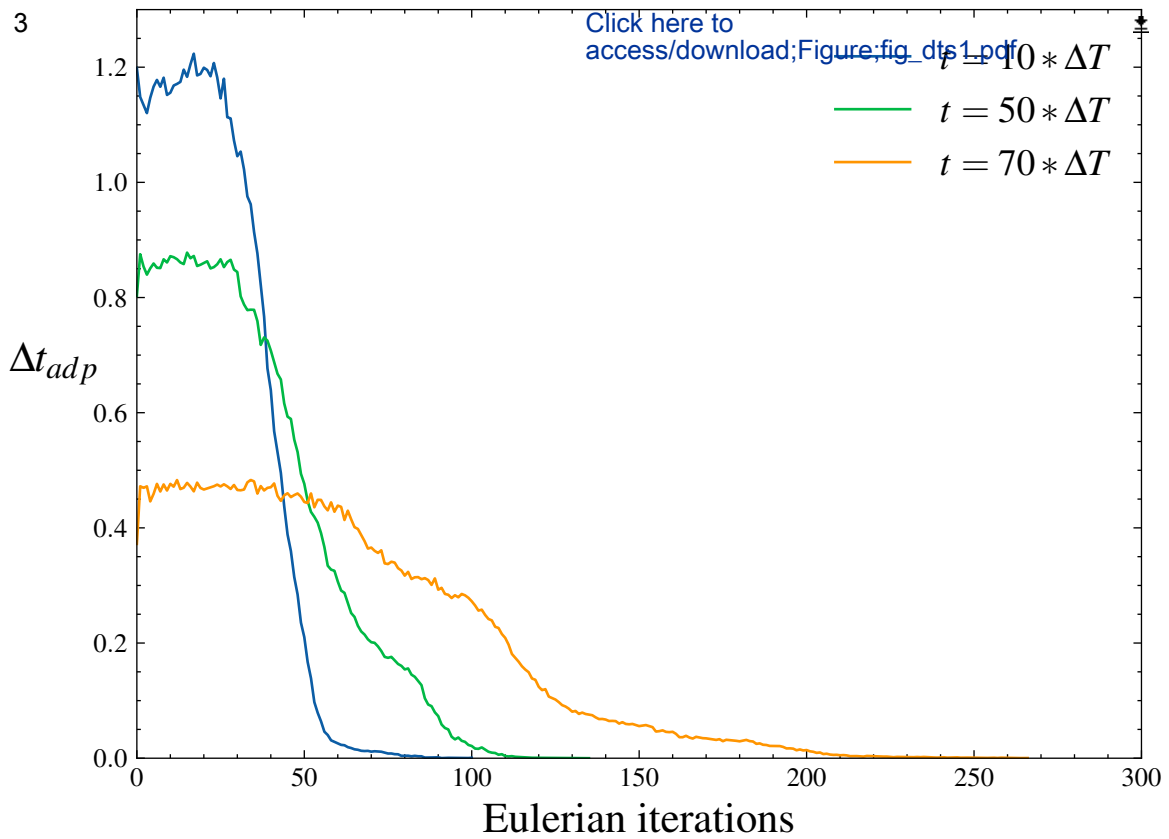
12
13 **Acknowledgement**
14
15

16 The work was inspired by H.L. Berk during Ge Wang worked with him at the University of
17 Texas. This work was supported by the National Natural Science Foundation of China under Grant
18 No. 12275013.
19

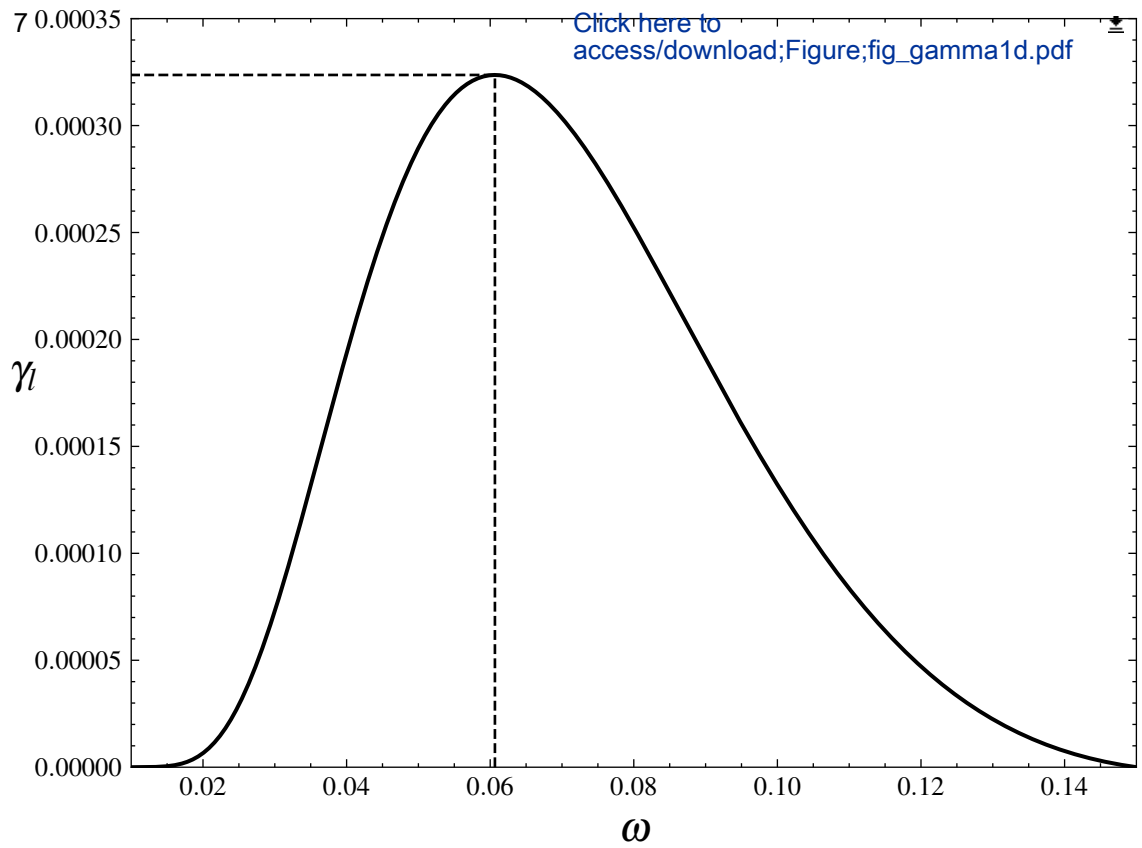
- 20 [1] L. Chen, F. Zonca, Physics of Alfvén waves and energetic particles in burning plasmas, Rev. Mod. Phys. 88
21 (2016) 72.
22 [2] G. Wang, H. Berk, B. Breizman, L.-J. Zheng, Frequency chirping in the Alfvén continuum, Nuclear Fusion 58
23 (2018) 082014.
24 [3] G. Wang, H. Berk, Simulation and theory of spontaneous TAE frequency sweeping, Nucl. Fusion 52 (2012)
25 094003.
26 [4] G. Wang, H. Berk, Model for spontaneous frequency sweeping of an Alfvén wave in a toroidal plasma, Com-
27 munications in Nonlinear Science and Numerical Simulation 17 (2012) 2179–2190.
28 [5] A. Fasoli, C. Gormenzano, H. L. Berk, B. Breizman, S. Briguglio, D. S. Darrow, N. Gorelenkov, W. W. Heid-
29 brink, A. Jaun, S. V. Konovalov, R. Nazikian, J.-M. Noterdaeme, S. Sharapov, K. Shinohara, D. Testa, K. Tobita,
30 Y. Todo, G. Vlad, F. Zonca, Chapter 5: Physics of energetic ions, Nuclear Fusion 47 (2007) S264–S284.
31 [6] B. T. Tsurutani, E. J. Smith, Postmidnight chorus: A substorm phenomenon, Journal of Geophysical Research
32 (1896–1977) 79 (1974) 118–127.
33 [7] S. Kasahara, Y. Miyoshi, S. Yokota, T. Mitani, Y. Kasahara, S. Matsuda, A. Kumamoto, A. Matsuoka,
34 Y. Kazama, H. U. Frey, V. Angelopoulos, S. Kurita, K. Keika, K. Seki, I. Shinohara, Pulsating aurora from
35 electron scattering by chorus waves, Nature 554 (2018) 337–340.
36 [8] G. D. Reeves, H. E. Spence, M. G. Henderson, S. K. Morley, R. H. W. Friedel, H. O. Funsten, D. N. Baker, S. G.
37 Kanekal, J. B. Blake, J. F. Fennell, S. G. Claudepierre, R. M. Thorne, D. L. Turner, C. A. Kletzing, W. S. Kurth,
38 B. A. Larsen, J. T. Niehof, Electron Acceleration in the Heart of the Van Allen Radiation Belts, Science 341
39 (2013) 991–994.
40 [9] R. M. Thorne, W. Li, B. Ni, Q. Ma, J. Bortnik, L. Chen, D. N. Baker, H. E. Spence, G. D. Reeves, M. G.
41 Henderson, C. A. Kletzing, W. S. Kurth, G. B. Hospodarsky, J. B. Blake, J. F. Fennell, S. G. Claudepierre, S. G.
42 Kanekal, Rapid local acceleration of relativistic radiation-belt electrons by magnetospheric chorus, Nature 504
43 (2013) 411–414.
44 [10] G. Chen, L. Chacón, A multi-dimensional, energy- and charge-conserving, nonlinearly implicit, electromagnetic
45 Vlasov–Darwin particle-in-cell algorithm, Computer Physics Communications 197 (2015) 73–87.
46 [11] J. Xiao, J. Liu, H. Qin, Z. Yu, A variational multi-symplectic particle-in-cell algorithm with smoothing functions
47 for the Vlasov–Maxwell system, Physics of Plasmas 20 (2013) 2517–.
48 [12] J. XIAO, H. QIN, Explicit structure-preserving geometric particle-in-cell algorithm in curvilinear orthogonal
49 coordinate systems and its applications to whole-device 6D kinetic simulations of tokamak physics, Plasma
50 Science and Technology 23 (2021) 055102.
51 [13] H.-s. Xie, D. Banerjee, Y.-k. Bai, H.-y. Zhao, J.-c. Li, BORAY: A ray tracing code for various magnetized
52 plasma configurations, Computer Physics Communications 276 (2022) 108363.
53 [14] D. NUNN, A NOVEL TECHNIQUE FOR THE NUMERICAL-SIMULATION OF HOT COLLISION-FREE
54 PLASMA - VLASOV HYBRID SIMULATION, J. Comput. Phys. 108 (1993) 180–196.
55
56
57

- [15] Y. Katoh, Y. Omura, Electron hybrid code simulation of whistler-mode chorus generation with real parameters in the Earth's inner magnetosphere, *Earth, Planets and Space* 68 (2016) 192.
- [16] X. Tao, A numerical study of chorus generation and the related variation of wave intensity using the DAWN code, *J. Geophys. Res. Space Physics* 119 (2014) 3362–3372.
- [17] M. K. Lillej, B. N. Breizman, S. E. Sharapov, Destabilizing Effect of Dynamical Friction on Fast-Particle-Driven Waves in a Near-Threshold Nonlinear Regime, *Physical Review Letters* 102 (2009) 195003.
- [18] B. N. Breizman, Nonlinear travelling waves in energetic particle phase space, *Nuclear Fusion* 50 (2010) 084014.
- [19] H. Hezaveh, Z. Qu, B. Layden, M. Hole, Impact of energetic particle orbits on long range frequency chirping of BGK modes, *Nuclear Fusion* 57 (2017) 126010.
- [20] H. Hezaveh, Z. S. Qu, B. N. Breizman, M. J. Hole, Long range frequency chirping of Alfvén eigenmodes, *Nuclear Fusion* 60 (2020) 056014.
- [21] H. Hezaveh, Z. S. Qu, M. J. Hole, R. L. Dewar, Theoretical description of chirping waves using phase-space waterbags, *Plasma Physics and Controlled Fusion* 63 (2021) 065008.
- [22] C. M. Bender, S. A. Orszag, Advanced Mathematical Methods for Scientists and Engineers I, Springer New York, New York, NY, 1999. URL: <http://link.springer.com/10.1007/978-1-4757-3069-2>. doi:[10.1007/978-1-4757-3069-2](https://doi.org/10.1007/978-1-4757-3069-2).
- [23] F. Arecchi, R. Bonifacio, Theory of optical maser amplifiers, *IEEE Journal of Quantum Electronics* 1 (1965) 169–178.
- [24] J. Zheng, G. Wang, B. Li, A hamiltonian theory for whistler chorus wave in the magnetosphere, submitted to *Physics of Plasmas* (2023).
- [25] T. Shiroto, A. Matsuyama, M. Yagi, A charge-momentum-energy-conserving 1D3V hybrid Lagrangian–Eulerian method for Vlasov–Maxwell system, *Journal of Computational Physics* 469 (2022) 111522.
- [26] T. Nogi, Y. Omura, Nonlinear Signatures of VLF-Triggered Emissions: A Simulation Study, *JGR Space Physics* 127 (2022) e2021JA029826.
- [27] K. Imadera, Y. Kishimoto, D. Saito, J. Li, T. Utsumi, A numerical method for solving the Vlasov–Poisson equation based on the conservative IDO scheme, *Journal of Computational Physics* 228 (2009) 8919–8943.
- [28] E. Sonnendrücker, J. Roche, P. Bertrand, A. Ghizzo, The Semi-Lagrangian Method for the Numerical Resolution of the Vlasov Equation, *Journal of Computational Physics* 149 (1999) 201–220.
- [29] G.-H. Cottet, Semi-Lagrangian particle methods for high-dimensional Vlasov–Poisson systems, *Journal of Computational Physics* 365 (2018) 362–375.
- [30] C. F. Kennel, H. E. Petschek, Limit on stably trapped particle fluxes, *Journal of Geophysical Research* 71 (1966) 1–28.
- [31] C. F. Kennel, Velocity Space Diffusion from Weak Plasma Turbulence in a Magnetic Field, *Physics of Fluids* 9 (1966) 2377.
- [32] R. E. Denton, Electron density in the magnetosphere, *J. Geophys. Res.* 109 (2004) A09215.
- [33] S. P. Gary, Theory of Space Plasma Microinstabilities, Cambridge University Press, 1993. doi:[10.1017/CBO9780511551512.008](https://doi.org/10.1017/CBO9780511551512.008).
- [34] Y. Omura, Y. Katoh, D. Summers, Theory and simulation of the generation of whistler-mode chorus, *J. Geophys. Res. Space Phys.* 113 (2008).
- [35] X. Tao, F. Zonca, L. Chen, Y. Wu, Theoretical and numerical studies of chorus waves: A review, *Science China Earth Sciences* 63 (2020) 78–92.

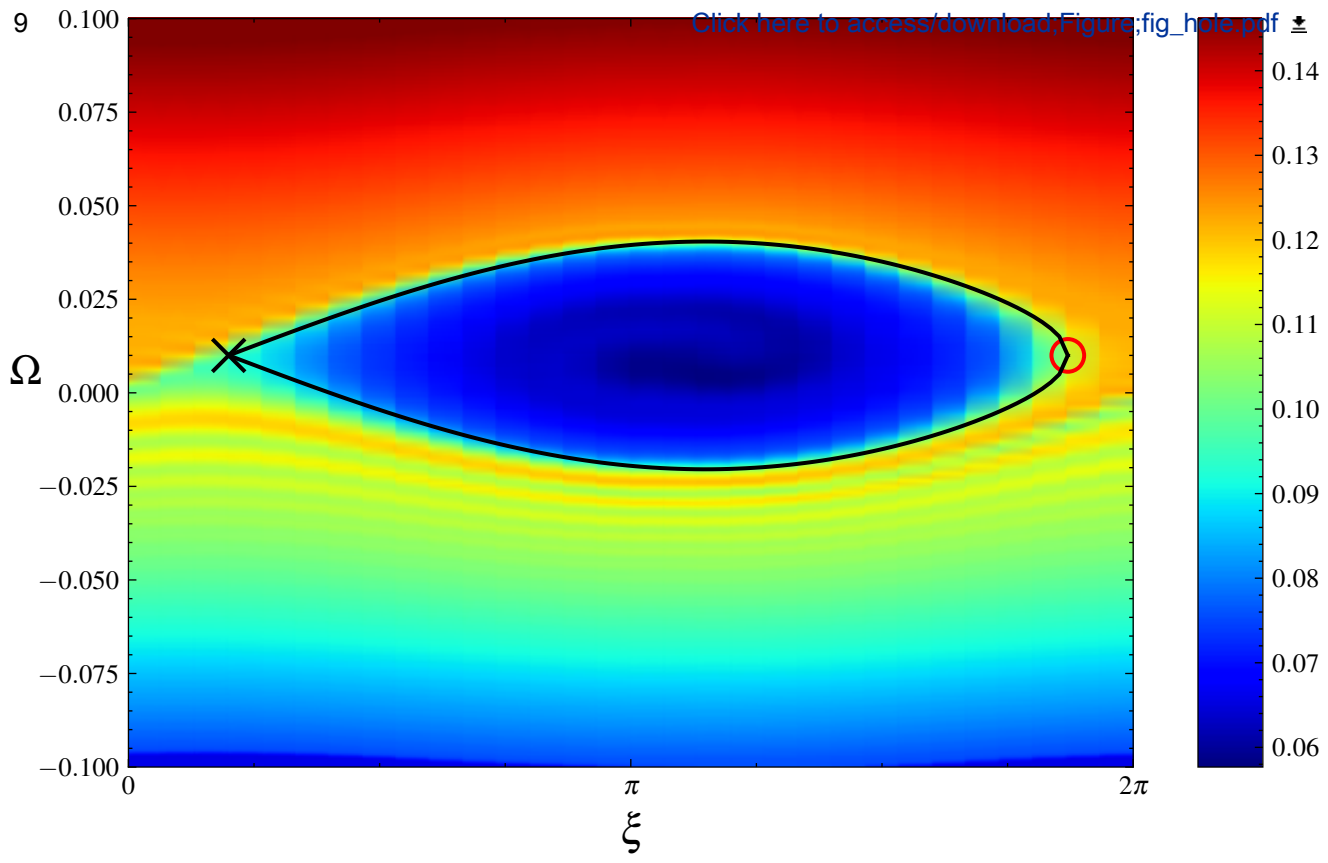


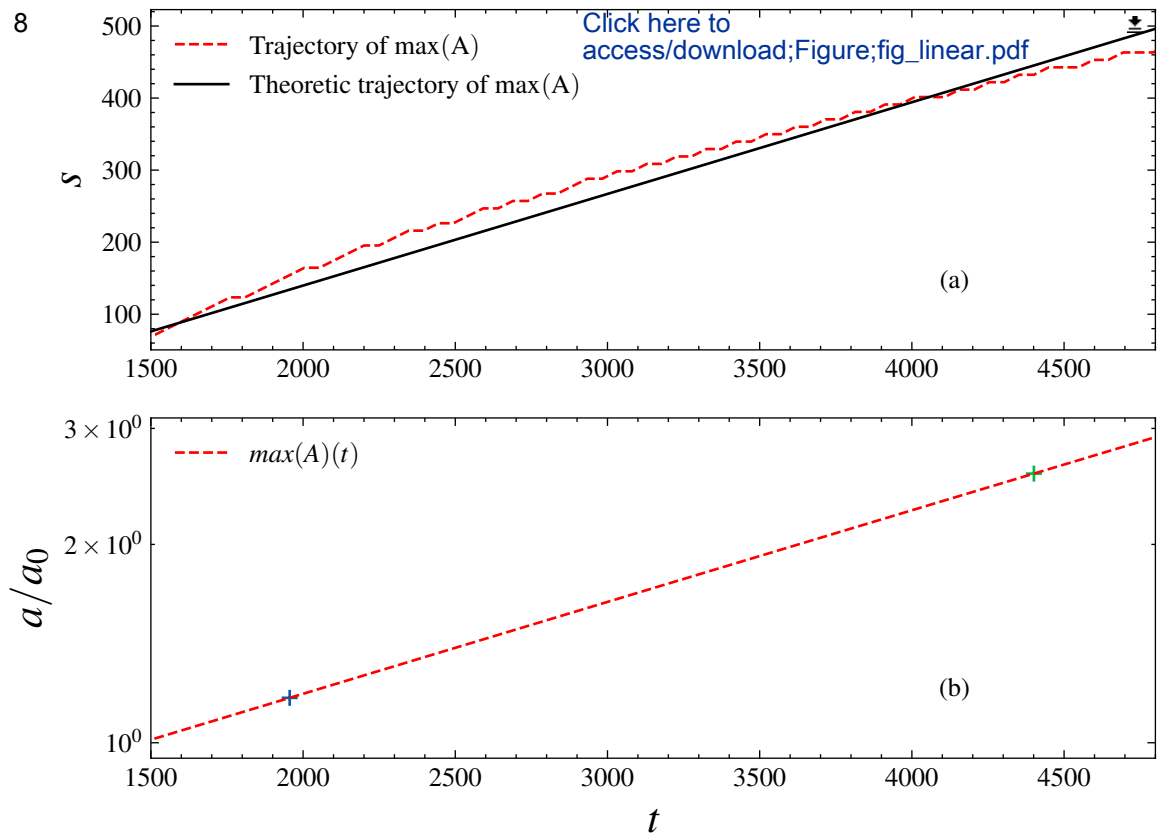


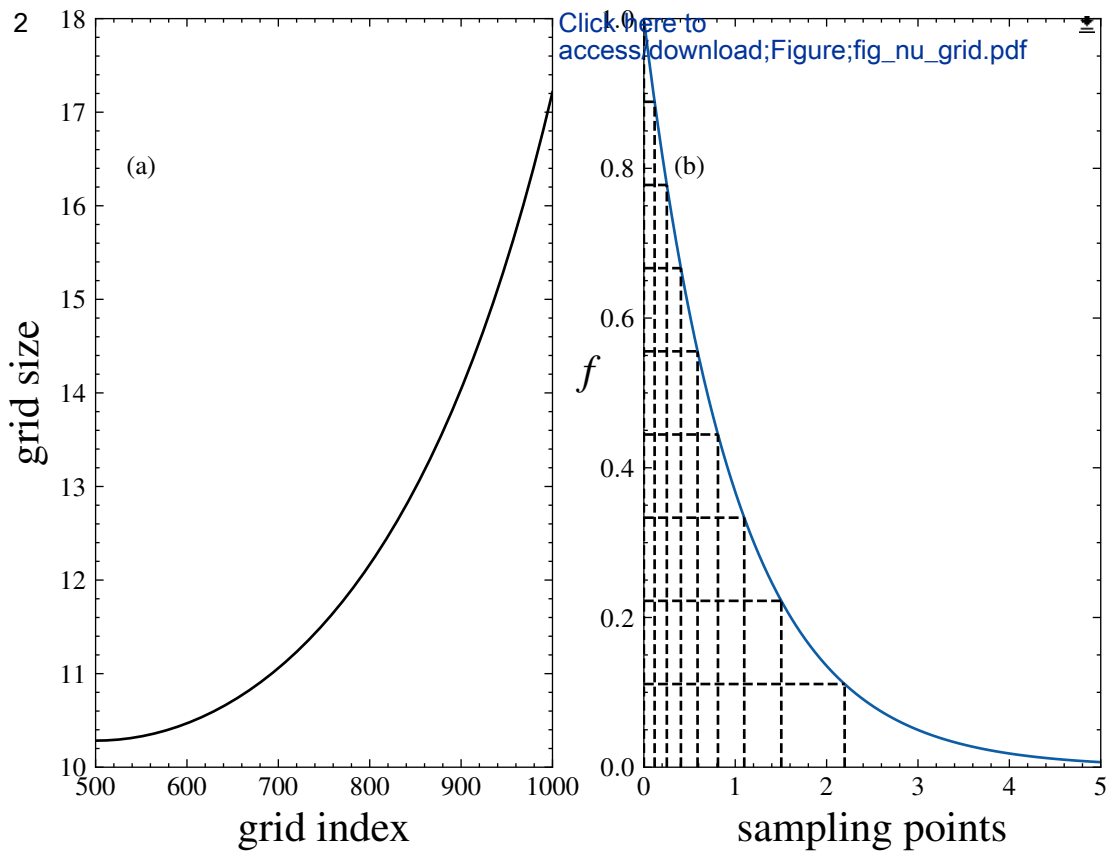
Click here to
access/download;Figure;fig_gamma1d.pdf



Click here to access/download Figure; fig_hole.pdf

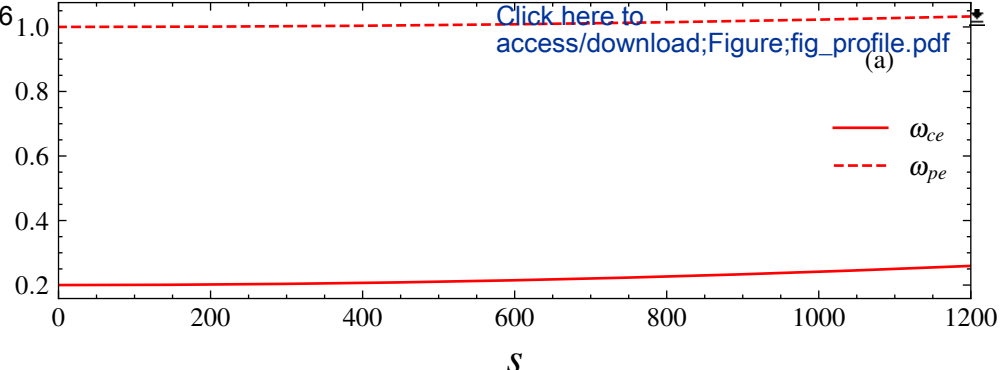






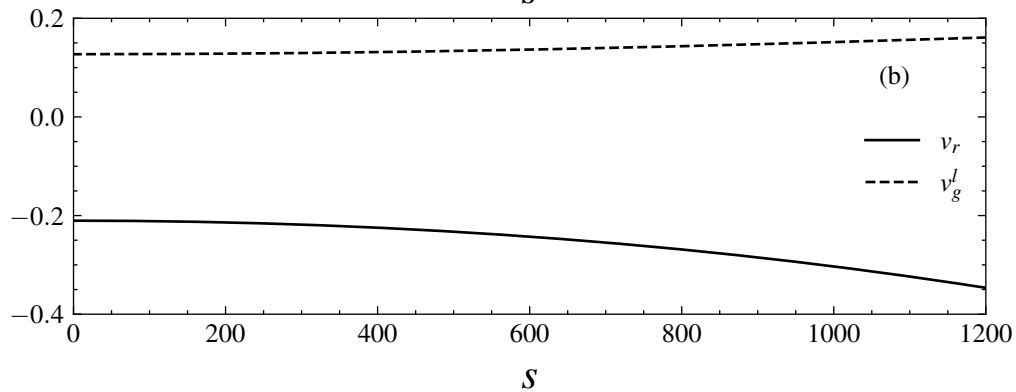
[Click here to
access/download;Figure;fig_profile.pdf](#)

(a)



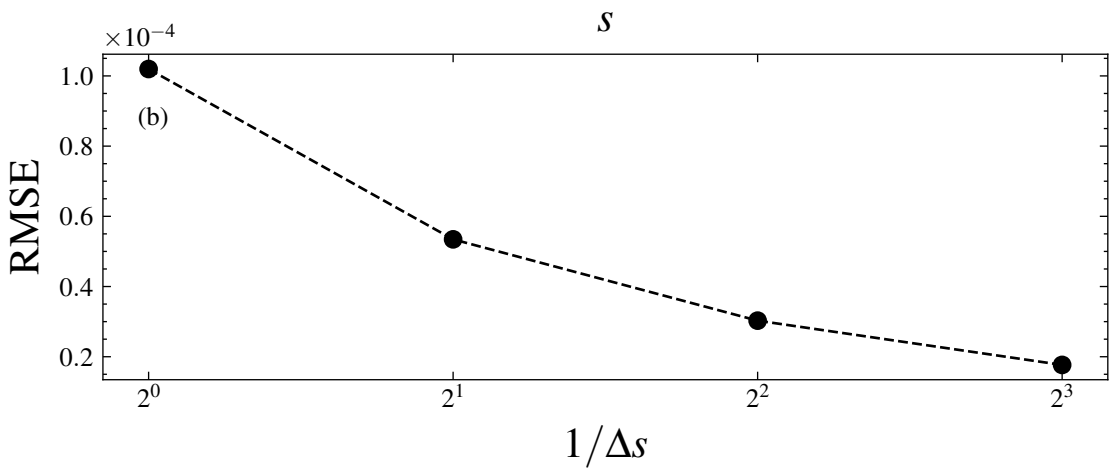
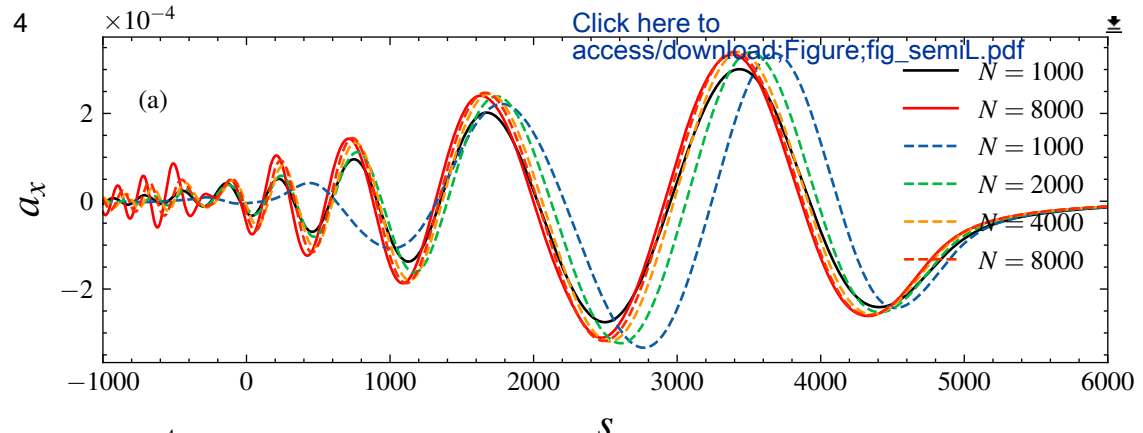
S

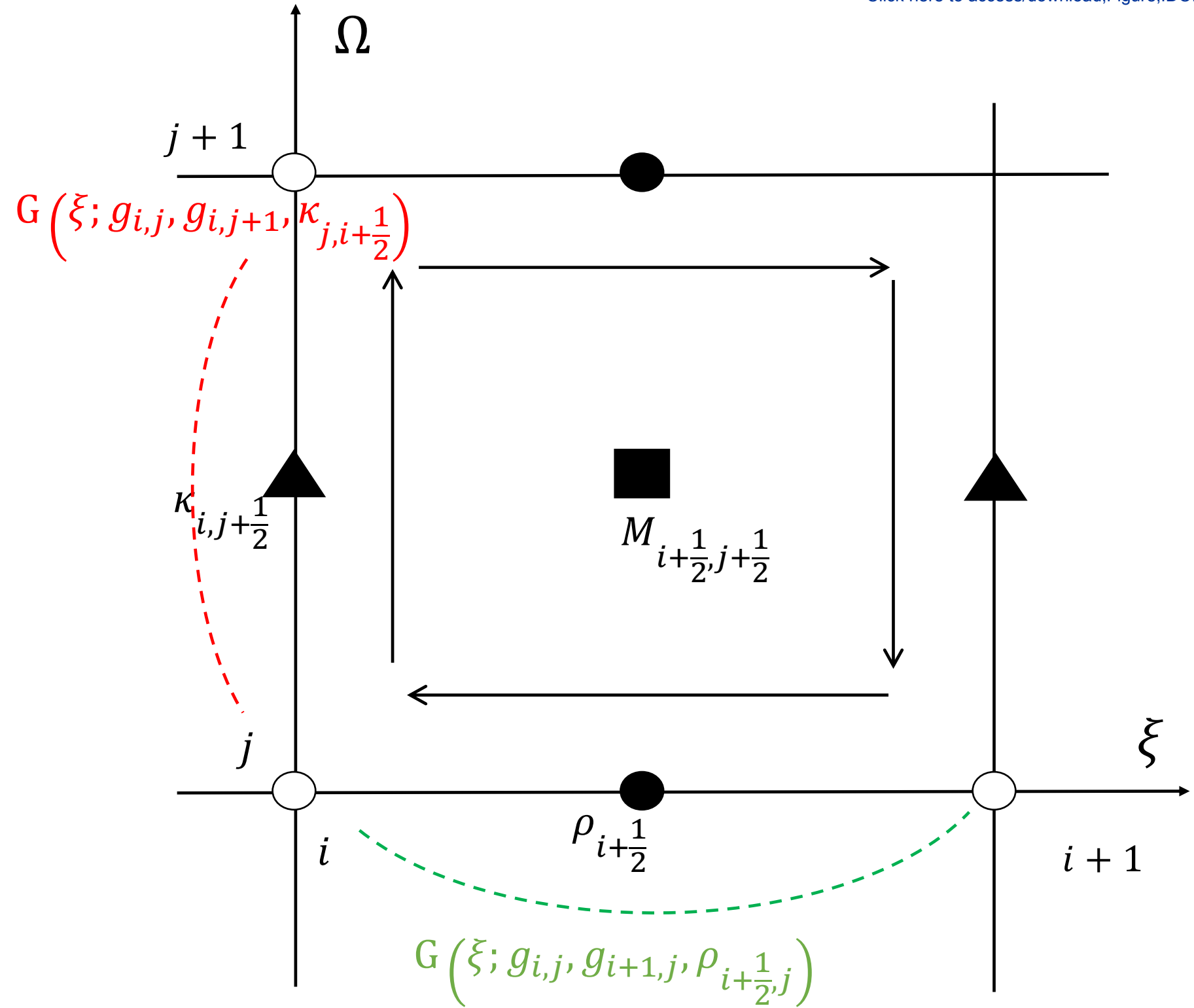
(b)



S

Click here to
access/download Figure;fig_semiL.pdf





Declaration of interests

The authors declare that they have no known competing financial interests or personal relationships that could have appeared to influence the work reported in this paper.

The authors declare the following financial interests/personal relationships which may be considered as potential competing interests: